34, 481 (1892); also R. Landauer, J. Appl. Phys. **23**, 779 (1952). The present formula [Eq. (12)] has recently been derived independently by L. Genzel and T. P. Martin, Phys. Status Solidi **51**, 91 (1972), and by F. L. Galeener, Phys. Rev. Lett. **27**, 421 (1971).

[11]W. Cochran, Z. Kristallogr. **112**, 465 (1959); also A. S. Barker, Jr., Phys. Rev. 136, A1290 (1964).

[12]W. G. Spitzer and D. A. Kleinman, Phys. Rev. **121**, 1324 (1961).

[13]A. S. Barker, Jr., Phys. Rev. **165**, 917 (1968).

[14]D. D. Manchon (unpublished). See also D. D. Manchon and P. J. Dean, in *Proceedings of the Tenth International Conference on the Physics of Semiconductors* (U. S. AEC, Oak Ridge, Tenn., 1970), p. 760.

[15]This suggestion was first made by D. D. Manchon and P. J. Dean (unpublished).

[16]N. F. Mott and I. N. Sneddon, *Wave Mechanics and Its Applications* (Clarendon, Oxford, England, 1948), Sec. 32.

[17]The correct treatment of the polarizability of a bound charge in a dielectric with dispersion is extremely complicated and parameter sensitive even in the continuum model. See, for example, J. J. O'Dwyer and H. H. Nickle, Phys. Rev. B **2**, 5063 (1970).

[18]A. S. Barker, Jr. and R. Loudon, Rev. Mod. Phys. **44**, 18 (1972).

[19]C. H. Henry, J. J. Hopfield, and L. C. Luther, Phys. Rev. Lett. **17**, 1178 (1966).

[20]A. S. Barker, Jr. (unpublished).

PHYSICAL REVIEW B VOLUME 7, NUMBER 6 15 MARCH 1973

Alfvén-Wave Propagation and Damping in Pyrolytic and Single-Crystal Graphite*

Alan R. Krauss† and Jacek K. Furdyna
Department of Physics, Purdue University, Lafayette, Indiana 47907
(Received 6 July 1972)

A systematic study of Alfvén-wave propagation was carried out at 35 GHz in pyrolytic and single-crystal graphite by means of microwave transmission and reflection experiments at 4.2 and 77 K. The amplitude and phase of the propagating wave were measured independently, yielding values of the collision frequency and the effective-carrier mass density at 4.2 K. These values were in reasonable agreement with theoretical and previously reported experimental values, although there was some evidence that the collision time is magnetic field dependent. The measured mass densities for pyrolytic and single-crystal samples were the same within experimental error. Transmission measurements were carried out as a function of angle between the applied magnetic field and the direction of propagation, revealing a quasi-two-dimensional behavior of the mass density, characteristic of graphite. On the other hand, these measurements indicate little anisotropy in the scattering rate. Experiments performed at 77 K yield a slightly higher value of the mass density, in agreement with the nonparabolic energy-band structure predicted by the Slonczewski–Weiss model. Very pronounced oscillatory structure observed in Alfvén-wave damping at 4.2 K in the case of single-crystal graphite is identified as Shubnikov–de Haas oscillations associated with *both* majority and minority carriers. The single-crystal data also revealed a small oscillation in the transmitted phase.

I. INTRODUCTION

Semimetals with equal electron and hole concentrations (such as bismuth, antimony, and graphite) are capable of supporting wave propagation of a type similar to that described by Alfvén[1] for two-component gaseous plasmas. The first direct observations of Alfvén-wave transmission in solids were made by Williams[2] for bismuth and antimony by detecting the interference between microwave leakage around the sample and transmission through the sample. Transmission-amplitude measurements have been used to determine collision frequencies in bismuth and the transmission envelope has exhibited Shubnikov–de Haas oscillations in damping.[3] The transmitted phase has also displayed Shubnikov–de Haas effects due to variation in carrier concentration.[4]

In comparison with bismuth, graphite has received relatively little attention. Because of its greater carrier concentration and higher collision frequency (both are an order of magnitude larger), graphite is considerably less transparent, requiring either very high fields, thin samples, or sensitive apparatus to detect transmission. However, the constant-energy surfaces of the carriers in graphite are parallel to a common symmetry axis and the effects associated with Fermi-surface anisotropy are considerably simplified. Graphite is therefore a material of interest in the study of electromagnetic-wave propagation in compensated solids.

Alfvén waves were first observed in graphite by Surma, Furdyna, and Praddaude[5] by means of geometric interference in a thin flake mounted inside a microwave reflection cavity. The experimental geometry was that of the "fast" Alfvén wave, i.e., the plane of polarization (direction of $\vec{E}_{rf}$) was perpendicular to both the dc magnetic field and wave vector $\vec{q}$, and the magnetic field

was rotated relative to the symmetry axis c. Transmission was studied in thicker samples of pyrolytic graphite at fields up to 140 kG by Furdyna and Krauss[6] in an experiment in which the Faraday geometry ($\vec{B} \parallel \vec{q} \parallel \vec{c}$) was employed. In this geometry the fast and slow Alfvén waves have the same dispersion relation.

This paper presents a study of the propagation of slow Alfvén waves ($\vec{E}$ in the $\vec{B}$, $\vec{q}$ plane) in graphite. The effect of the anisotropy characteristic of this material on Alfvén-wave dispersion and damping is analyzed theoretically. A systematic experimental investigation of Alfvén-wave transmission in single-crystal and pyrolytic graphite is carried out as a function of the angle between $\vec{B}$ and $\vec{q}$ in the low-field (1 to 20-kG) region. Information obtained from the data concerning mass and collision anisotropy, quantum oscillations, and the general problem of wave propagation in a quasi-two-dimensional medium are discussed.

II. THEORY

The different species of carriers in the solid behave as free-carrier plasmas if the interband and phonon interaction effects may be neglected. Anisotropic energy surfaces complicate the orientational behavior of the wave solutions, but within the limits of the effective-mass approximation it is possible to use the classical electromagnetic-wave equation to derive the relation between frequency and the propagation constant (dispersion relation).

The solution to the wave equation may be written in the form

$$A\eta^4 + B\eta^2 + C = 0 \ , \tag{1}$$

where $\eta = q/q_0$ is the index of refraction and A, B, and C are algebraic functions of the tensor components of the dielectric function.[7] The dielectric tensor $\overleftrightarrow{K}$ is related to the conductivity tensor $\overleftrightarrow{\sigma}$ by the expression $\overleftrightarrow{K} = \overleftrightarrow{K}_L - i\overleftrightarrow{\sigma}/\omega\epsilon_0$. In a conducting medium, the lattice contribution $\overleftrightarrow{K}_L$ is much smaller than the free-carrier term and will be ignored.

In the spirit of regarding the various carrier species in a solid as independent free-particle plasmas, the equation of motion may be written for a single species in the presence of a dc magnetic field B_0,

$$\overleftrightarrow{m} \cdot \frac{\partial \vec{v}}{\partial t} = Q\vec{E} + Q\vec{v} \times \vec{B} - \overleftrightarrow{\nu} \cdot \overleftrightarrow{m} \cdot \vec{v} \ , \tag{2}$$

where $Q = \pm |e|$ is the charge, $\overleftrightarrow{m}$ is the effective mass, $\overleftrightarrow{\nu}$ is the collision frequency, $\vec{v}$ is the drift velocity of the carrier, and $\vec{B} = \vec{B}_0 + \vec{B}_{rf}$ is the total magnetic field. Under the conditions of the experiment $B_{rf} \ll B_0$ and effects associated with $\vec{B}_{rf}$ are small. The quantity $\vec{B}_{rf}$ will therefore be ignored in Eq. (2). In an isotropic medium, the mass and collision frequency are scalars.

If the current density $\vec{J}(r)$ depends only upon the instantaneous value of $\vec{E}(r)$, the conductivity is said to be local and is related to the current density by means of Ohm's law. The current density, in turn, is given by

$$\vec{J} = \sum_\alpha n_\alpha e \vec{v}_\alpha \ , \tag{3}$$

where the summation extends over the various carrier species, n_α is the concentration of that species, and $\vec{v}_\alpha$ is the solution of Eq. (2).

The assumption that conductivity in graphite is local is justified experimentally by the fact that effects related to nonlocal conductivity have never been observed in this material; and theoretically, by the fact that although the parameters for graphite come close to satisfying the criteria usually associated with nonlocal conductivity, calculation has shown that no nonlocal effects are to be expected.[8]

A. Isotropic Conductivity

The choice of coordinate system most convenient for an anisotropic solid depends on the geometry of the Fermi surface. However, a convenient choice for the isotropic solid is one in which the z axis is along the magnetic field and the propagation vector $\vec{q}$ is in the x-z plane. In this coordinate system, $q_x = q\sin\theta$, $q_y = 0$, $q_z = q\cos\theta$, $B_x = B_y = 0$, and $B_z = B_0$, where $B_0 = |\vec{B}_0|$. Writing Eq. (2) in component form and evaluating the secular determinant, the conductivity arising from a single carrier species is found to be

$$\overleftrightarrow{\sigma} = \frac{ne^2}{D} \begin{bmatrix} \gamma^2 & QB_0\gamma & 0 \\ -QB_0\gamma & \gamma^2 & 0 \\ 0 & 0 & D/\gamma \end{bmatrix} \ , \tag{4}$$

where n is the carrier concentration and

$$\gamma = (\nu + i\omega)m \ , \quad D = \gamma^3 + \gamma e^2 B_0^2 \ . \tag{5}$$

It is convenient to define the cyclotron frequency $\omega_c = eB_0/m$ and the plasma frequency $\omega_p = (ne^2/m\epsilon_0)^{1/2}$. Wave propagation with the characteristic Alfvén-wave dispersion and little damping will exist under the conditions $\nu/\omega_c \ll 1$, $\omega/\omega_c \ll 1$. Expanding Eq. (4) in these quantities, the dielectric constant for a medium with two carrier species may be written $K_{xz} = K_{zx} = K_{yz} = K_{zy} = 0$, $K_{yy} = K_{xx}$,

$$\begin{aligned} K_{xx} &= \left(1 - i\frac{\nu}{\omega}\right)\left(\frac{\omega_{pe}^2}{\omega_{ce}^2} + \frac{\omega_{ph}^2}{\omega_{ch}^2}\right) \ , \\ K_{xy} &= \left(2\nu + i\frac{\omega^2 - \nu^2}{\omega}\right)\left(\frac{\omega_{pe}^2}{\omega_{ce}^3} - \frac{\omega_{ph}^2}{\omega_{ch}^3}\right) \ , \\ K_{zz} &= -\frac{\omega + i\nu}{\nu^2 + \omega^2}\,\frac{\omega_{pe}^2 + \omega_{ph}^2}{\omega} \ , \end{aligned} \tag{6}$$

where the subscripts e and h refer to electrons

and holes, respectively. The correct Alfvén-wave dispersion relation will result if ν is defined as an "average" of the electron and hole collision frequency[9]

$$\nu = (\nu_e m_e + \nu_h m_h)/(m_e + m_h) \ . \tag{7}$$

K_{xy} is roughly a factor of ω/ω_c smaller than K_{xx}. Since the two quantities K_{xx} and K_{xy} appear together in the dispersion relation, K_{xy} will be ignored. There are then two solutions to Eq. (1):

$$\eta_+^2 = \left(1 - i\,\frac{\nu}{\omega}\right)\left(\frac{\omega_{pe}^2}{\omega_{ce}^2} + \frac{\omega_{ph}^2}{\omega_{ch}^2}\right) \ , \tag{8}$$

$$\eta_-^2 = \eta_+^2/\cos^2\theta \ .$$

In the limit of small ν/ω they may be written

$$q_+ = (\omega/v_a)\,(1 - i\,\nu/2\omega) \tag{9a}$$

and

$$q_- = q_+/\cos\theta \ , \tag{9b}$$

where $v_a = B_0/(\mu_0 M)^{1/2}$ is termed the Alfvén velocity and $M = n_e m_e + n_h m_h$ is the carrier mass density. The damping is described by the imaginary part of the propagation constant, which is smaller than the real part provided $\nu/\omega < 1$. When this condition is satisfied, waves corresponding to both solutions propagate with relatively little damping. The phase velocities corresponding to q_+ and q_- are v_a and $v_a\cos\theta$, respectively. These modes are termed the fast and slow Alfvén waves and are analogous to ordinary and extraordinary waves in birefringent media.

B. Anisotropic Conductivity

The expressions derived so far ignore one of the salient features of graphite—its anisotropy. The Fermi surfaces of graphite are roughly ellipsoidal, with a conical elongation at the tips. However, wave propagation should be relatively unaffected by the behavior at the ends of the majority surfaces because of the low density of states in that region. Aside from giving rise to cyclotron-resonance harmonics, warping of the electron-surface cross section does not appear to substantially affect the orbital masses, provided an ellipsoidal model of suitable anisotropy is used.[10] Consequently, it is possible to describe propagation effects in terms of ellipsoidal Fermi surfaces for the two carriers.

It is convenient to take the hexagonal axis in the z direction. Then, because of the trigonal symmetry in the basal plane, $m_x = m_y$. We will define transverse and longitudinal masses: $m_t = m_x = m_y$, $m_l = m_z$. A similar designation is used to define transverse and longitudinal collision frequencies, ν_t and ν_l. A second subscript will be used to designate electrons or holes as necessary. The ratio of longitudinal to transverse effective mass is 146 : 1 for both electrons and holes.[10] For arbitrary anisotropy, the mass density M becomes a function of the principal masses. The form of this relation depends on the geometry of the Fermi surfaces and the experimental configuration.

A complication occurs in graphite because the transverse mass is a function of k_z. In order to obtain the Alfvén-mass density, it is necessary to integrate over the mass distribution:

$$M = \sum_\alpha \int_{\mathrm{FS}} n_\alpha(k_z) m_\alpha(k_z)\, dk_z = n_e \overline{m}_e + n_n \overline{m}_n \ . \tag{10}$$

The summation extends over the ellipsoids and the integration is along the zone edge. The integrated mass density has been calculated by Dresselhaus and Dresselhaus.[11]

In general, it is also necessary to allow for anisotropy in the scattering frequency. Although reasonable results have been obtained by Soule, McClure, and Smith[10] by assuming isotropic scattering, recent conductivity measurements by Spain[12] indicate a conductivity ratio approaching 10^5 at 4.2 K. This ratio is far too large to be explained on the basis of mass anisotropy alone.

Anisotropic scattering rates may be incorporated into the theory for graphite by proceeding directly from Eq. (2), provided a suitable coordinate system is chosen. Since the free-carrier contribution to the dielectric constant is very large, the refractive index is also large; incident radiation is bent very strongly toward the normal upon entering the medium. Graphite cleaves easily in the basal plane, but cannot be either cleaved or ground in any other plane without causing considerable damage. Experimentally, the surface of the sample is therefore always in the basal plane and the direction of propagation is always along the c axis. Consequently, $\tilde{\mathrm{q}}$ corresponds to a principal axis of the ellipsoidal Fermi surface. Since the coordinate system is chosen with $\tilde{\mathrm{q}}$ along the z axis, the coordinate axes correspond to the principal ellipsoid axes in k space. The effective-mass tensor is diagonalized in this coordinate system, and it will be assumed that the collision frequency is also diagonalized.

The dispersion relation is obtained from the wave equation by setting $q_x = q_y = 0$, $q_z = q$ and evaluating the secular determinant. An expression in the form of Eq. (1) results, with

$$A = K_{zz} \ ,$$

$$B = K_{xz}^2 - K_{zz}(K_{xx} + K_{xy}) + K_{yz}^2 \ , \tag{11}$$

$$C = \det\left|\overleftrightarrow{\mathrm{K}}\right| \ .$$

By rotating the magnetic field in the xz plane so that $B_{0x} = B_0\sin\theta$, $B_{0y} = 0$, $B_{0z} = B_0\cos\theta$, and considering only one ellipsoid at a time, Eq. (2) separates into three scalar equations. The calculation

of $\vec{K}$ proceeds as before and the expressions are presented in the Appendix. For the extreme case of a cylindrical Fermi surface ($m_c = m_t/\cos\theta$) in a compensated medium, a rather interesting result is found. There are no longer two distinct solutions with the anisotropy of M merely included in the angular dependence of the isotropic solutions [Eqs. (9)]. Instead, the two solutions are identical to first order in ω/ω_c and have the same angular dependence as the slow Alfvén wave in an isotropic medium:

$$q_\pm = \omega(\mu_0 M_t)^{1/2}/B_0\cos\theta\ , \tag{12}$$

where $M_t = (n_e m_{te} + n_h m_{th})$. The calculation is shown in the Appendix.

The angular behavior of the cyclotron mass m_c in graphite is the same as that of the infinite cylinder over a wide angular range, as shown in Fig. 1. Equation (12) is expected to apply in this range to Alfvén-wave propagation in graphite. The phase velocities of the two solutions, calculated numerically using the exact expressions for $\vec{K}$ given in the Appendix, are shown as a function of angle for various mass anisotropies in Fig. 2. The plots are polar, θ being the angle between $\vec{B}_0$ and $\vec{q}$, with the radius representing the phase velocity. As the mass anisotropy is increased, the angular behavior of the fast wave approaches that of the slow wave until the two appear identical for the anisotropy corresponding to graphite.

1. Shubnikov-de Haas Phenomena

Quantization of the energy levels in a magnetic field results in an oscillatory collision frequency which in turn affects the Alfvén-wave damping. A complete treatment of the effects of collisions is outside the intended scope of this paper; it is sufficient to compare the observed oscillatory periods with the known Shubnikov–de Haas periods.

There is a slight oscillation in the Fermi energy when a Landau level crosses the Fermi surface. In a compensated semimetal such as graphite, the Fermi level is determined by the requirement that the number of electrons equals the number of holes. This number varies as the density of states changes under the influence of the magnetic field. The effect is more pronounced at high magnetic fields and leads to a departure from periodicity of the Shubnikov–de Haas extrema in addition to that produced by spin splitting of the Landau levels. In semimetals and intrinsic semiconductors, this oscillation of the Fermi level produces an oscillation in the carrier concentration and, for Alfvén waves, an oscillation in the mass density. The resultant oscillations in the Alfvén-wave dispersion have been observed in bismuth by Isaacson and Williams.[4]

A related mechanism which should be even more important in graphite is capable of producing the same apparent effect. In Eqs. (9) the real part of the propagation constant is independent of the collision frequency. However, this equation is an expansion to first order in ν/ω of Eq. (8). In the samples studied, the quantity ν/ω is of the order 0.3 to 0.5 and the collision-dependent second-order term is not negligible. Retaining the second-order term, Eq. (8) may be expanded to give the expressions

$$q_+ = (1 + \tfrac{1}{8}\nu^2/\omega^2 - i\nu/2\omega)(\omega/B_0)(\mu_0 M)^{1/2}\ ,$$
$$q_- = q_+/\cos\theta\ . \tag{13}$$

If the collision frequency is oscillatory, the observed Alfvén-wave dispersion will also display weak oscillations associated with the ν^2/ω^2 term, with extrema corresponding to maxima in the scattering rate. This effect is more important in graphite than in bismuth because graphite has a much higher scattering frequency. The same effect has been analyzed for helicon waves and observed in highly doped InSb and InAs by Furdyna and Krauss.[13]

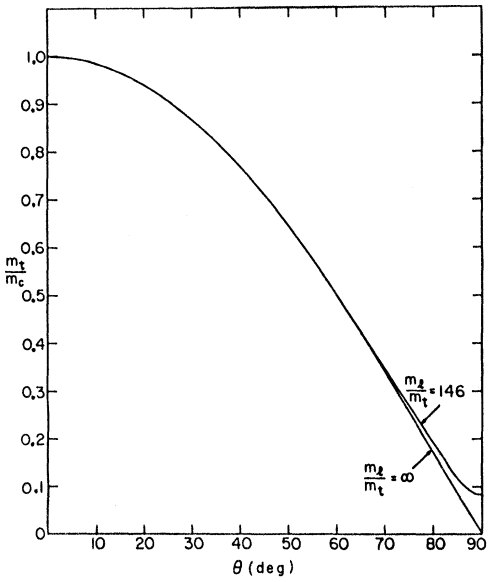

FIG. 1. Comparison of the orientational dependence of the cyclotron mass for an infinite circular cylinder with that for an ellipsoid with a mass anisotropy $m_l/m_t = 146$, corresponding to graphite.

III. EXPERIMENTAL PROCEDURE

A. Microwave Spectrometer

The simplest possible experimental arrangement for observing microwave transmission through a thin slab of material consists of a waveguide blocked by the slab, a klystron at one end of the waveguide, and a detector at the other end. How-

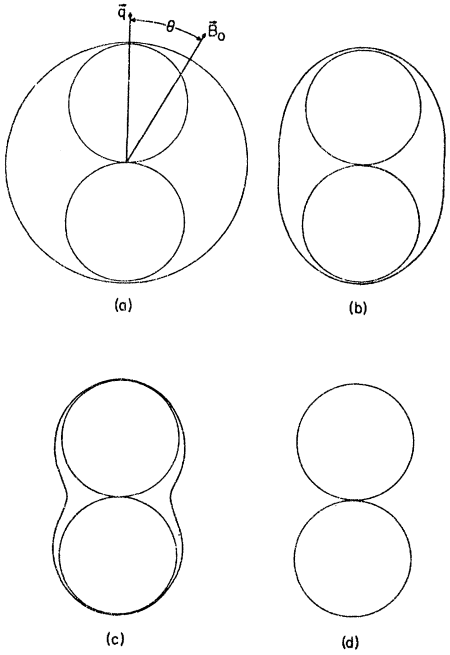

FIG. 2. Plots of the wave velocity for the two solutions to the Alfvén-wave dispersion relation. The plots are on a polar scale, the velocity being proportional to the radius and the angle between $\vec{B}$ and $\vec{q}$ being shown as θ. (a) Mass anisotropy $m_l/m_t=1$. (b) $m_l/m_t=2$. (c) $m_l/m_t=5$. (d) $m_l/m_t=146$. The two solutions are identical for the extreme anisotropy found in graphite. The difference shown for the solutions at $\theta=0°$ and $\theta=180°$ is caused by computer round-off error.

ever, if the sample is sufficiently opaque to prevent the observation of Fabry–Perot resonance, such a scheme will not yield any information on the phase of the transmitted wave. The addition of a bypass arm makes it possible to make continuous measurements of the phase change of a wave transmitted through an arbitrarily thick sample.[14] The bypass arm acts to produce an interference pattern in the same manner as deliberately introduced leakage employed in transmission experiments on bismuth. However, the phase and amplitude of the "leakage" may here be varied at will by means of a variable phase shifter and attenuator.

The amplitude of the transmitted wave depends on the transmission at the two interfaces t_1 and t_2 and the bulk attenuation coefficient β. The power loss corresponding to a single passage through a typical sample (ignoring multiple reflections) at 10 kG is ~70 dB. With approximately 10 mW of incident power, the spectrometer must be capable of detecting 10^{-9} W. This level is close to the theoretical minimum for microwave diodes and is far too small to be observed by simple video detection.

The spectrometer used was a modification of the 35-GHz spectrometer built by Evans[15] and shown in Fig. 3. It is capable of being used for both reflection and transmission experiments. When used in the transmission mode, it is equivalent to a Rayleigh interference bridge with the added refinements of a phase-locked-loop signal-klystron stabilizer, a resonant sample cavity, and superheterodyne detection.

In the transmission mode (shown in Fig. 3), microwave power modulation is achieved by the use of a ferrite modulator (Mod), while the hybrid ring $H1$ and E-H tuner are not functional. The transmitted signal is passed through a 60-dB isolation arm and mixed with power from the bypass arm at port 1 of hybrid ring $H2$. The signal at port 1 is divided between ports 2 and 4, while virtually none (– 30 dB) is communicated to port 3. Power from the local klystron enters port 3 and is divided between ports 2 and 4. Consequently, microwaves at the local-oscillator frequency ω_L and microwaves at the signal-oscillator frequency ω_S are mixed at diodes $D1$ and $D2$.

The resultant signal contains terms corresponding to a frequency $\omega_L - \omega_S$, which is adjusted to match the 30-MHz intermediate frequency of the tuned i.f. amplifier. Diodes $D1$ and $D2$ provide a balanced input to the i.f. amplifier, eliminating common mode noise. The i.f. amplifier output is then fed into a Princeton Applied Research HR-8 lock-in amplifier and from there to the y-axis drive of an x-y recorder. The x-axis drive is furnished by the magnet-sweep-control circuits. The modulation signal is derived from the lock-in reference output. The modulation frequency was typically 2.7 kHz when used with the ferrite modulator and 27 Hz when used for field modulation.

The output of the signal klystron was sampled via a 10-dB directional coupler by a Microwave Systems, Inc. klystron stabilizer and phase locked to a high-order harmonic of a quartz-crystal oscillator. Power from the local klystron was mixed with that of the signal klystron by diode $D3$. With the monitor/lock switch in the "lock" position the difference frequency was phase locked to a 30-MHz quartz-crystal oscillator by a modified Dymec oscillator synchronizer built by Evans.

The spectrometer can be converted to reflection operation merely by moving a small waveguide section in front of the 60-dB isolation arm from the position marked "xmission" to that marked "refl" in Fig. 3. The E-H tuner and hybrid ring $H1$ then become active parts of the microwave system, and the spectrometer functions as a balanced microwave bridge.

The sample cavity was suspended in a glass liquid-helium Dewar which was placed between the poles of the electromagnet. A Pyrex tube was used to keep liquid helium out of the cavity and the waveguide. Heat leakage between the atmosphere

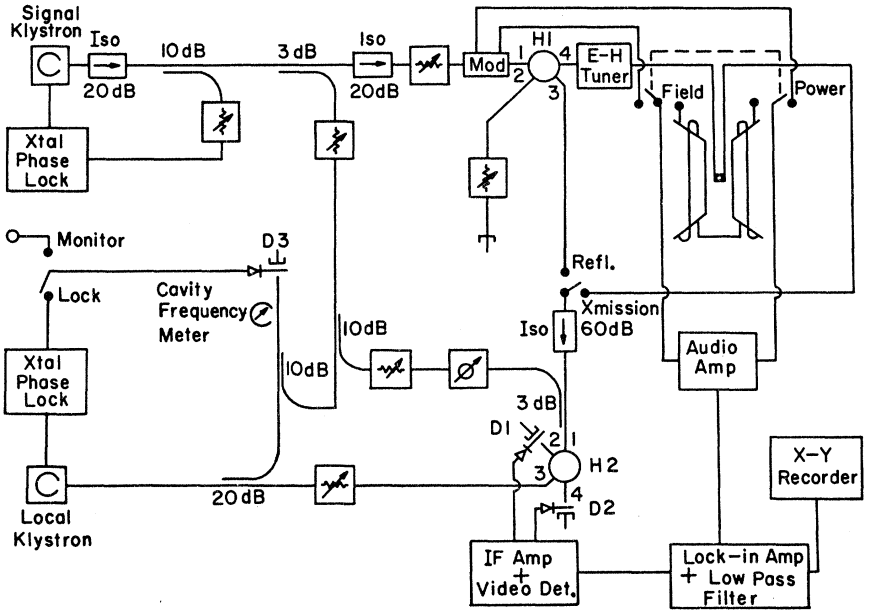

FIG. 3. Block diagram of the 35-GHz superheterodyne spectrometer, shown in the transmission mode.

and the cavity was reduced by placing a 2-ft. stainless-steel waveguide section between the cavity and the top of the Dewar.

An exploded view of the TE_{111} cylindrical cavity is shown in Fig. 4. A hole larger than the desired iris size, was drilled in the narrow wall of the stainless waveguide, which was silver soldered into a cylindrical brass block. The block, after machining, served as a mounting plate for the iris and one end of the cavity. The cavity was a coin-silver cylindrical waveguide soft soldered into a brass ring which provided a means of fastening the cavity to the mounting plates and furnished a threaded holder for the tuning screw. A cavity Q of 1000 was usually attainable, depending somewhat on the sample size when the graphite was placed inside the cavity for reflection measurements.

B. Sample Preparation and Mounting

For use in transmission, the sample was mounted on the exit iris. A copper washer thicker than the sample was soldered onto the back of the iris. The copper-plated sample was then tinned with Wood's metal and the entire assembly was heated until a uniform meniscus of Wood's metal formed between copper washer and sample. The back of the sample was covered with a thin indium-foil washer to prevent microwave leakage around the iris, and the iris assembly was mounted so that the sample was outside the cavity.

The sample itself was prepared in the form of a $\frac{1}{4}$-in. disk. A small piece of cellophane tape was pressed onto the sample and then removed, thereby cleaving the graphite. Often the sample would cleave in several places at once, producing a "staircase" effect on the surface which could be detected quite readily by observing with oblique lighting under a low-power microscope. When the surface was free of such structural defects, the sample would appear uniformly black. The centers were masked off with either a pair of small copper

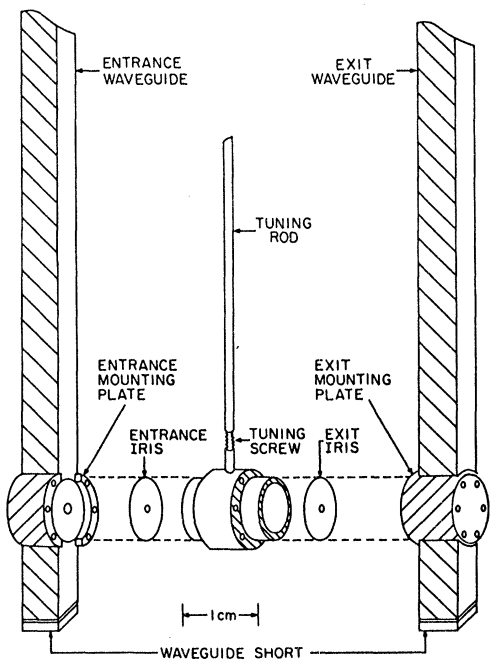

FIG. 4. Exploded view of the sample cavity. When used in reflection, the exit iris is replaced by a solid disk.

disks or pieces of cellophane tape and the sample was copperplated by either chemical deposition or electroplating methods.

The success in eliminating leakage could be ascertained before cooling to liquid-helium temperature by observing the transmission signal at 77 K. In all but the very thinnest samples, transmission through graphite was not observable at this temperature. Leakage around the sample appeared as a signal whose amplitude increased with magnetic field but whose phase was constant. Leakage elsewhere in the system (e.g., in an improperly shielded waveguide flange) appeared as a signal whose phase and amplitude were both field independent, and could be detected as a varying baseline when the phase shifter was rotated. This second type of leakage could not always be eliminated entirely, but was usually no more than a slight nuisance in that it required that the baseline be readjusted for each phase setting if more than one sweep of the magnetic field were to be recorded on a single chart.

Reflection samples were cut somewhat smaller than transmission samples and cleaved in the same manner. They were glued in the center of a thin copper disk which replaced the exit iris.

IV. RESULTS

A. Transmission

If the signal transmitted by a thin slab of graphite is mixed with a signal which has been fed around the sample by means of a bypass arm, constructive and destructive interference takes place as the phase of the transmitted wave varies with the magnetic field. Maxima occur when the transmitted and reference signals are in phase. When $\vec{B}_0 \parallel \vec{q}$, the phase angle between the two signals may be written

$$\varphi = \omega L/v_a - \Delta \,, \tag{14}$$

where Δ is the phase shift of the bypass arm and $\omega L/v_a$ is the phase shift associated with transmission through the sample (in rad). Maxima will recur whenever this phase angle is an integral multiple of 2π. Inserting Eqs. (9) into (14), we find an expression for the fringe index N:

$$N = (\mu_0 M)^{1/2} Lf/B_0 - \Delta/2\pi \,, \tag{15}$$

where $f = \omega/2\pi$ is the microwave frequency. It should be noted that the fringe index as used in Eq. (15) is not required to be an integer.

1. Pyrolytic Graphite

a. Phase. The signal transmitted by a slab of pyrolytic graphite is shown in Fig. 5. The dashed line indicates the envelope E_T. The sample corresponding to this figure is the thickest one for which transmission was observable. Phase information may be obtained directly from the positions of the extrema. A thinner sample would be required to observe transmission at substantially lower fields, but the spacing between the extrema would then increase and fewer phase data points would be available.

This difficulty may be overcome by using the phase shifter to vary the quantity Δ in controlled amounts. Figure 6 shows the superposition of traces obtained by varying Δ in increments of 90°. The crossing points obtained in this interferogram

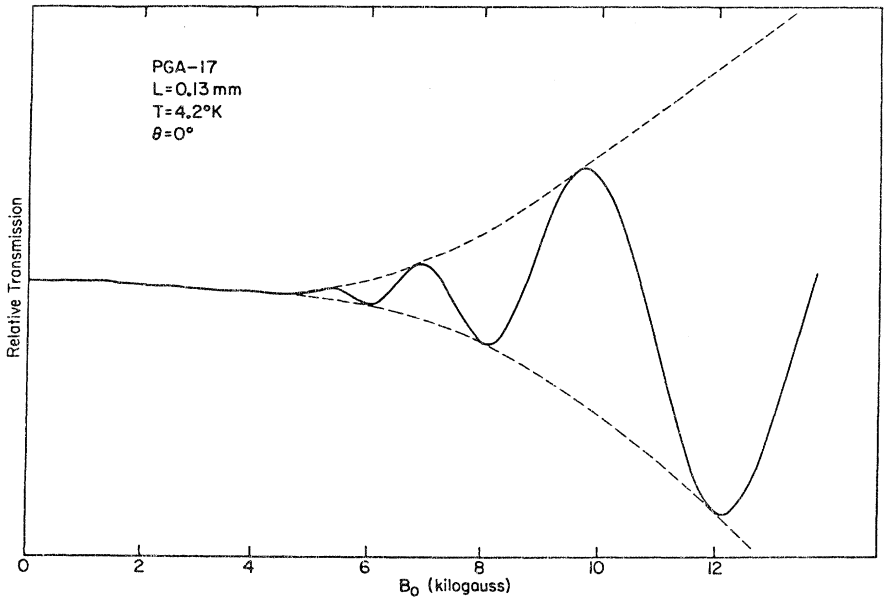

FIG. 5. Transmission through PGA−17. The transmitted signal beats with the bypass signal, producing an interference pattern. The envelope (dashed line) is swept out by rotating the phase shifter while at a given magnetic field, and is proportional to the transmitted power. The phase is determined by measuring the positions of the extrema.

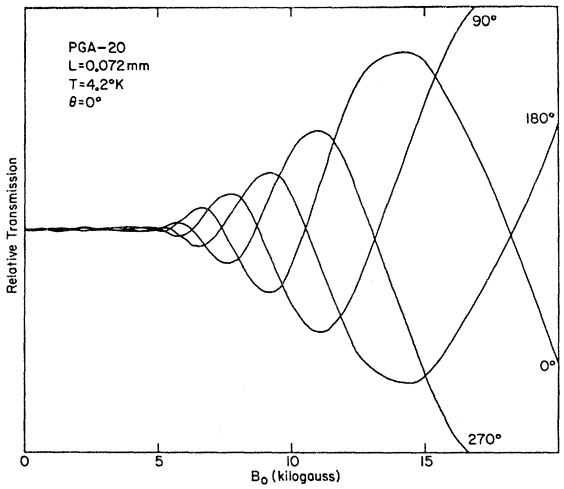

FIG. 6. Transmission interferogram for PGA – 20. A greater amount of phase data are obtainable by superposing several interference patterns, taken with different phase shifter settings.

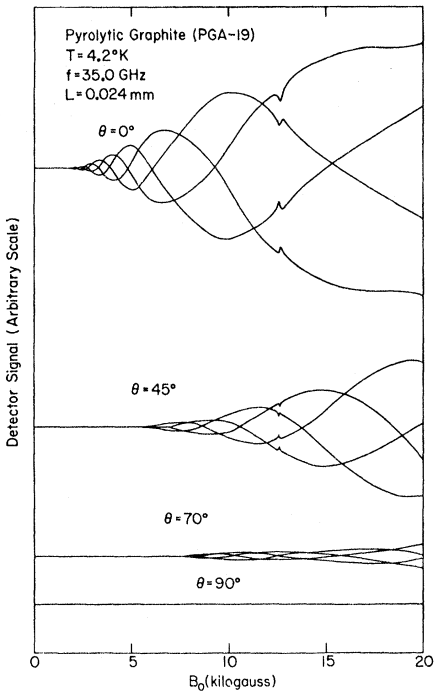

FIG. 7. The angular behavior of the interferogram for PGA – 19. The interference pattern expands and the envelope decreases as the magnetic field is rotated. The spike at 12.5 kG is caused by a spin resonance marker inside the cavity. It can be distinguished from phase interference effects by the fact that its position is independent of phase shifter settings.

can be used to measure the change in phase of the transmitted wave more accurately than the extrema. Similarly, by using eight equally spaced values of Δ, successive crossings correspond to phase increments of 45°. This procedure may be extended as far as desired; the resolution in the measurement of phase data is, in principle, determined only by the patience of the experimenter in recording successive traces. One important advantage of this method is that it can be used even when the total phase shift upon transmission is less than 360°.

The angular dependence of the interferogram is shown in Fig. 7 for sample PGA-19. As the angle between the c axis and the magnetic field increases, the period in $1/B_0$ between crossing points increases and the amplitude of the envelope at a given value of B_0 decreases. Figure 8 is a plot of fringe index as a function of inverse magnetic field for several orientations. Equation (15) leads us to expect the plot corresponding to $\theta = 0°$ to be a straight line with slope $(\mu_0 M)^{1/2}$. Linear behavior is indeed observed at high fields, but there is some departure from linearity for other samples at low-field values where the expansion in ω/ω_c used to derive Eq. (14) breaks down.

For materials such as graphite, with highly anisotropic Fermi surfaces, the Alfvén-wave dispersion for propagation along the symmetry axis is determined by the transverse mass density M_t. As the magnetic field is rotated, the Alfvén velocity is expected to vary as $\cos\theta$, except for angles approaching 90°. Defining an "effective" orientation-dependent mass density M_θ as the quantity determined by the slope of the lines in Fig. 8, we expect this quantity to satisfy the relation

$$M_\theta^{1/2} = M_t^{1/2}/\cos\theta \ . \tag{16}$$

The experimental values of the quantities $(M_t/M_\theta)^{1/2}$

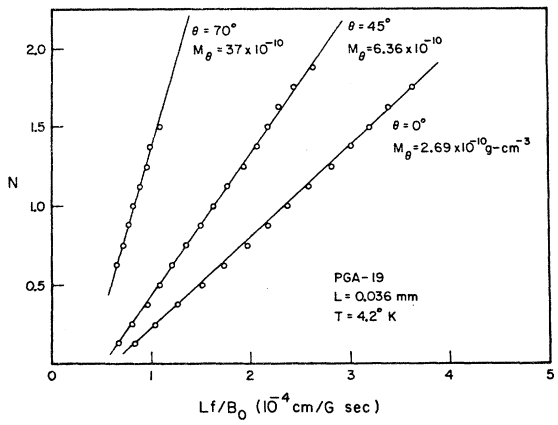

FIG. 8. Fringe index vs LfB_0^{-1} for PGA – 19. Because the collision frequency is low for this sample, the first-order terms in the expansion of the dispersion are adequate to describe the phase velocity. Consequently, the data fall on straight lines.

are plotted in Fig. 9 for five samples. The angular dependence is generally as expected, i.e., a cosine function (except for angles approaching 90°). The solid line indicates the angular variation of the cyclotron mass for the ellipsoidal Fermi surface. The scatter observed near 90° is probably a result of the poor quality of the data obtained in this region (see Fig. 7).

As expected, the two thinnest samples PGA-22 and PGA-24 were also the most transparent. Both exhibited transmission at liquid-nitrogen temperature, although there was sufficient microwave leakage around PGA-22 to cause some difficulty in analyzing the data. The results of the damping analysis show that, in spite of their excellent transparency, these two samples have a very high collision frequency. The relatively high collision frequency of these two samples, even at 4.2 K, can be understood in terms of the sample preparation procedure: The thicker samples were prepared by cleaving (literally peeling) thin sections until the remainder was of the desired thickness. Samples PGA-22 and PGA-24, however, were themselves the cleaved-off sections, and therefore more susceptible to damage.

The phase data are analyzed by means of Eq. (15) which is based on an expansion to first order in ν/ω_c of Eq. (8) and in which the transmitted phase is independent of the collision frequency. The quantity ν/ω_c is too large to be a good expansion parameter for samples PGA-22 and PGA-24. Consequently, the dispersion is in this case no longer linear in $1/B_0$ as it was in Fig. 8, but departs from linearity at low magnetic fields as shown in Fig. 10. This departure from linearity cannot be

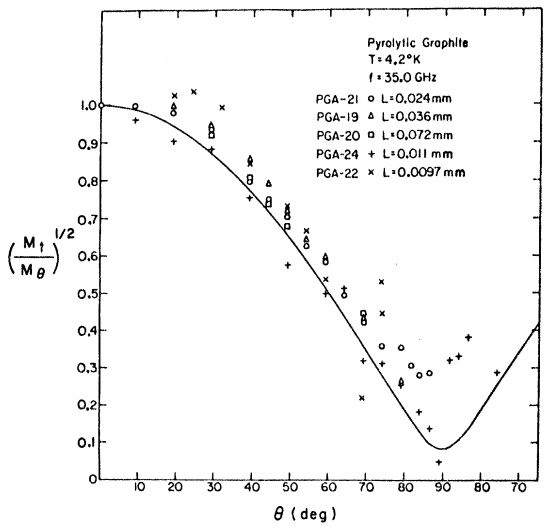

FIG. 9. Angular variation of the Alfvén-wave phase velocity (normalized to unity at $\theta = 0°$) for pyrolytic graphite.

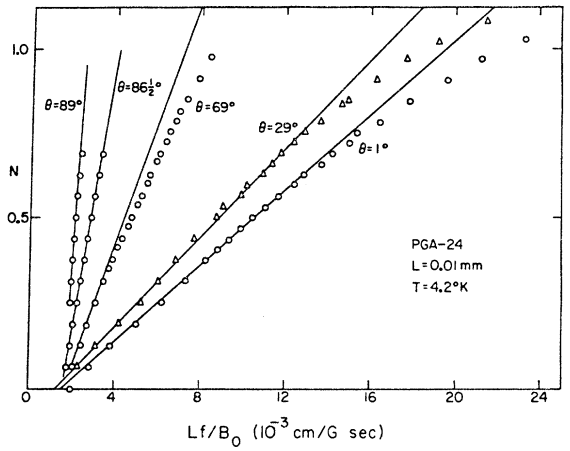

FIG. 10. Fringe index vs LfB^{-1} for PGA-24. Because of the high collision frequency, the data depart from linearity at low magnetic fields.

ascribed to nonlocal behavior since nonlocal conductivity requires a very *long* mean-free path and a very *low* collision frequency.

The experimental phase shift for samples PGA-22 and PGA-24 is shown in Fig. 11 in comparison with the theoretical phase shift computed numerically for several values of collision frequency, using the exact expressions for the dielectric tensor. On the basis of this figure, we may estimate the collision frequency to be between 10^{11} and 10^{12} sec^{-1} for PGA-24 at 4.2 K. The vertical positioning of the experimental data in the figures is arbitrary, since only the relative phase is measured. The data points are shifted vertically so that the "knees" of the experimental and theoretical curves coincide. The liquid-nitrogen phase data for sample PGA-24 (Fig. 12) exhibit an even more striking departure from linearity, corresponding to a collision frequency greater than 10^{12} sec^{-1}. This

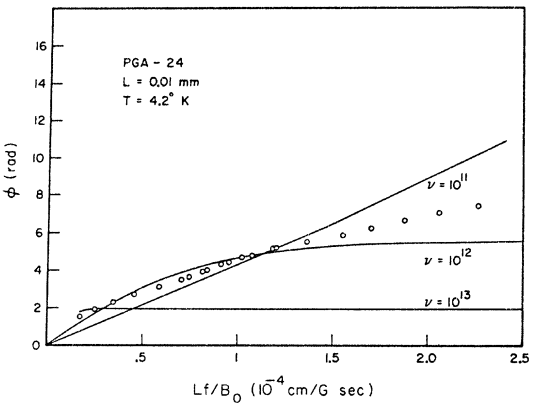

FIG. 11. Experimental phase shift for PGA-24. Comparison with the theoretical plots (solid lines) shows that $10^{11} < \nu < 10^{12}$ sec^{-1}.

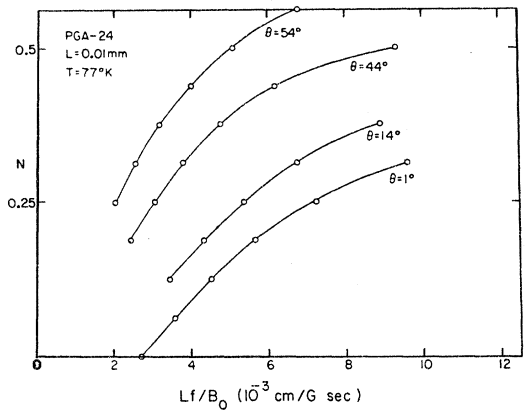

FIG. 12. Angular dependence of the fringe index for PGA-24 at 77 °K.

variation with temperature is in general agreement with the results of McClure.[16]

When $\nu/\omega_c > 1$, as it is in PGA-24 at 77 K, the value of M obtained from the phase analysis no longer corresponds to the mass density, but would be below the value obtained at 4.2 K. The experimental value obtained for PGA-24 at 77 K is, however, substantially higher than the value obtained at 4.2 K. Magnetoresistance and Hall measurements[16,17] have shown that the carrier concentration is nearly constant for temperatures up to 120 K. The increased experimental value must therefore correspond to an increased mass density associated with the nonparabolic nature of the energy bands.

Useful information about the band structure might be obtained by observing the Alfvén-wave dispersion as a function of temperature. Unlike the quantities measured in dc experiments, the dispersion is, to a first approximation, independent of collision frequency. The mass density measures the product of the carrier concentration with mass rather than the quotient found in magnetoresistance measurements. A comparison of the two types of data could reduce the ambiguity of some of the quantities previously measured by dc methods alone. The experimental disadvantage lies, of course, in the fact that, because of the increased collision frequency, graphite is quite opaque at temperatures significantly above 4.2 K and transmission is not readily observable except in very thin samples. This difficulty should be reduced by carrying out experiments in the millimeter and submillimeter wave region.

b. Damping. If the quantity ν/ω_c is small and the collision frequency is isotropic, ν can be determined by measuring the envelope of the transmission data. If $\nu/\omega_c \ll 1$, the damping of the transmitted wave is given by the imaginary part of Eqs. (9). For samples significantly thicker than the skin depth, the (complex) amplitude of the transmitted wave is given by the expression

$$E_T = t_1 t_2 e^{iqL} E_0 , \tag{17}$$

where L is the sample thickness, t_1 and t_2 are the transmission coefficients of the two interfaces, and E_0 is the amplitude of the incident microwave electric field. The quantity $t_1 t_2$ may be written in the form[18] $4B_0 f(\theta)/c(\mu_0 M)^{1/2}$, where the quantity $f(\theta)$ is a function of magnetic field orientation, the form of the dependence differing for the two possible linear polarizations. Writing $q = \alpha + i\beta$, we find

$$\mathrm{Re}(E_T) = [4B_0 f(\theta)/c(\mu_0 M)^{1/2}] e^{-\beta L} , \tag{18}$$

where $\beta = (\mu_0 M)^{1/2}\nu/2B_0 g(\theta)$ is the Alfvén-wave damping coefficient and $g(\theta) = \cos\theta$ for the slow Alfvén wave (pertinent to the present experiment). For the fast wave it becomes a function of both θ and the mass anisotropy. A plot of $\ln(E_T/P_0)$ vs $1/B_0$ would give a straight line (assuming ν independent of B_0) with a slope of $-\frac{1}{2}(\mu_0 M)^{1/2}\nu L/g(\theta)$; the collision frequency could then be determined from such a plot. A similar procedure was first suggested by Marston and Kao[19] for reflection experiments, and was later adapted by Isaacson and Williams[3] and by Furdyna and Krauss[6] to measure the collision frequency in slab transmission experiments in bismuth and graphite, respectively.

If, however, the quantity ν/ω_c is greater than unity (low fields or high collision frequency) the expansion used to derive Eq. (18) will diverge. The quantity ν_s determined from experiment on the basis of the above slope analysis

$$\nu_s = -2s(\mu_0 M)^{-1/2}\cos\theta/L \tag{19}$$

[where s is the $\ln(E_T/B_0)$ vs $1/B_0$ slope] will then no longer correspond to the actual collision frequency ν. The full expressions for $\overleftrightarrow{K}$ derived in the Appendix are in that case necessary to calculate the damping. The results of this calculation are shown in Fig. 13 for several values of ν. For the values of ν most pertinent to this experiment, $10^{10} < \nu < 10^{11}$, the plot of β vs $1/B_0$ does become linear at high fields, and the quantity ν_s is a reliable indication of the collision frequency. For substantially higher collision frequencies, the calculated results show that ν_s is no longer equal to the actual collision frequency and ceases to have any useful physical interpretation.

Figure 14 shows experimental values of $\ln(E_T/B_0)$ vs $1/B_0$ plotted in the manner of Fig. 13 (with the y axis inverted) for several orientations of the magnetic field. The vertical position is arbitrary, since the experiment only measures relative transmission. The solid line corresponds to the theoretical plot for $\theta = 0°$, calculated with the value $\nu = 4\times10^{10}$ sec^{-1}, obtained from the slope of the ex-

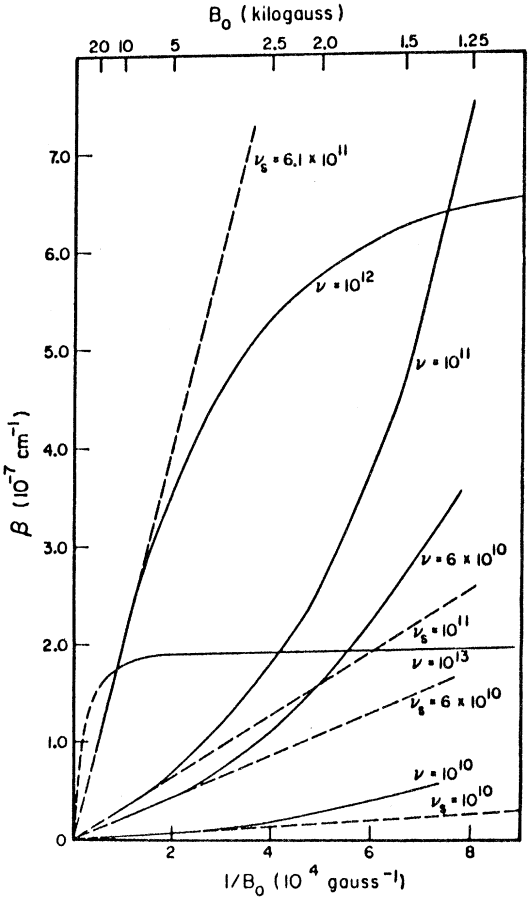

FIG. 13. Theoretical plot of β vs $1/B_0$. For $\nu < \omega$, the curves are concave upward and the high-field slopes correspond to the collision frequency. For $\nu > \omega$, the curves are concave downward and the high-field slopes no longer correspond to the collision frequency.

perimental data at high fields. The dashed line is the linear extrapolation of this high-field behavior. While the theoretical behavior does depart from linearity at lower fields, the experimental data depart significantly more, indicating a possible field dependence of the collision frequency.

If the collision frequency is isotropic, the local theory shows that, except for angles approaching 90°, the high-field slope obtained from Fig. 14 should vary as $(\cos\theta)^{-1}$, and the experimental quantity ν_s will be independent of the angle, provided $\nu/\omega_c \ll 1$ and $\omega/\omega_c \ll 1$. If the collision frequency is not isotropic, ν_s becomes a complicated function of the magnetic field orientation and of the longitudinal and transverse collision frequencies. The quantity ν_s may, however, be regarded as an "effective" collision frequency and be compared with the value theoretically obtained from a β-vs-$1/B_0$ plot calculated for given ν_l and ν_t. The sensitivity of the quantity ν_s to the anisotropy ratio R_ν

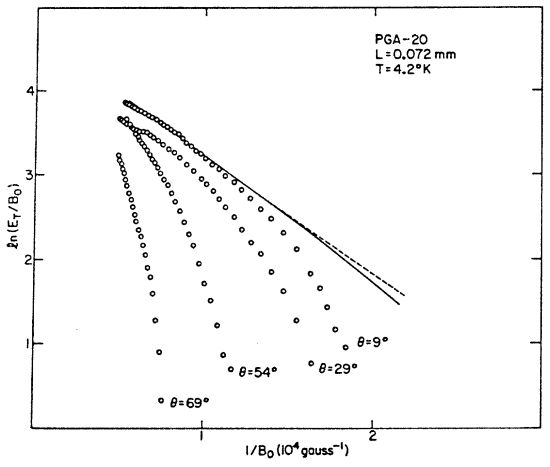

FIG. 14. $\ln E_T/B_0$ vs $1/B_0$ for PGA-20. In the limit $\nu/\omega_c \ll 1$, the vertical axis is $-\beta$ and the plot is comparable with Fig. 13 with the scale inverted. The high-field slope (dashed line) corresponds to $\nu = 4\times10^{10}$ sec^{-1}. At low fields the data diverge from the plot expected for this constant value of ν (solid line).

$= \nu_l/\nu_t$ depends on the value of ν_t. The samples studied had transverse collision frequencies in the vicinity of 10^{11} sec^{-1} as determined by the slope analysis of the data for $\theta = 0°$. Figure 15 shows that for this value of ν_t, ν_s should have a significant angular dependence for $\theta < 70°$ if the collision anisotropy ratio R_ν is greater than 10.

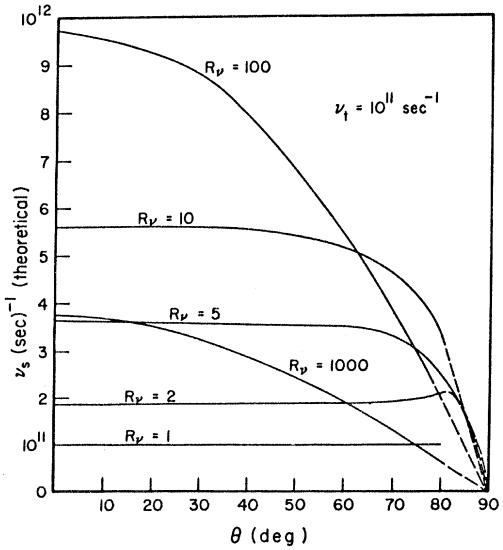

FIG. 15. Theoretical plot of ν_s vs θ for several values of collision anisotropy ratio $R_\nu = \nu_l/\nu_t$ showing that with $\nu_t = 10^{11}$ sec^{-1}, the quantity ν_s is relatively sensitive to collision anisotropy. The plot is extrapolated between 80° and 90° because of computer round-off error in this range.

The angular dependence of ν_s is shown in Fig. 16 for three samples. The data are consistent with a collision anisotropy of less than 10, in agreement with the findings of Soule, McClure, and Smith.[10] Although there is substantial experimental scatter, it is quite clear that this value is far less than the value of approximately 1000 observed by Spain.[12] We observe in the context of this result that presence of microcracks between basal plane layers could have serious effect on the longitudinal conductivity measured by Spain, although they would have no effect on microwave measurements if the crack spacing were greater than the carrier mean-free path.

2. *Single-Crystal Graphite*

Most of the purified single-crystal samples were rather small and generally unsuited to mounting for transmission experiments. The unpurified samples, on the other hand, were large enough to be mounted and produced data similar to that found for pyrolytic material but of much poorer quality. One of the largest purified single crystals, however, was successfully mounted. The results obtained from that sample will be dealt with in this subsection.

The sample was designated SCG-6 and originally came from the same piece as SCG-7, which was studied by means of the reflection experiment to be discussed in Sec. IV B. Sample SCG-6 was only slightly larger than the exit iris required for optimum cavity coupling. Consequently, some leakage occurred. The leakage, however, was not severe enough to cause difficulty except at the highest gain settings. Even at these gain settings it was possible to obtain data for the two-phase settings in which the bypass signal was at 90° to the leakage signal. Since the phase of the leakage was field independent, a flat baseline would then result and the crossing points of the interferogram could be used to measure the phase of the transmitted wave. The sample, although relatively thick (0.61 mm), proved to be more transparent than most of the thinner pyrolytic samples.

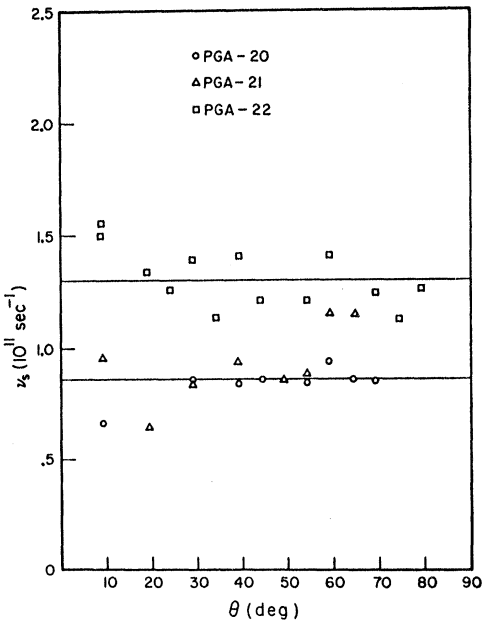

FIG. 16. Experimental plot of ν_s vs θ for three samples with $\nu_t \simeq 10^{11}$ sec^{-1}. The data are consistent with a collision-frequency anisotropy <10.

The transmission interferograms are shown in Figs. 17 and 18, the latter being an enlargement of the low-field data of Fig. 17. Instead of the monotonic field dependence observed for pyrolytic samples, the envelope (dashed line) is now marked by a series of "kinks" or "dimples." Only two phase settings are shown in Fig. 18 because the envelope was distorted by leakage at other settings. The other settings, however, showed that the features do not shift their position as the phase shifter is rotated, thereby indicating that the observed "kinks" correspond to an increased damping and are not associated with the phase of the transmitted wave.

The plot of $\ln(E_T/B_0)$ vs $1/B_0$ (Fig. 19) displays these features even more clearly than the interferogram. The four minima marked by arrows coincide with the four "kinks" observed in the single-crystal Alfvén-wave data of Surma, Furdyna, and Praddaude,[5] which were ascribed to the Shubnikov–de Haas effect. By fitting an average straight line through the high-field region of Fig. 19, a value of 3.85×10^{10} sec^{-1} was obtained for the collision frequency. This low value further indicates the high quality of the specimen.

The minima appearing in Fig. 19, starting at the high-field end of the data, have been designated by consecutive integers N. If all the minima correspond to Shubnikov–de Haas extrema of a single carrier, the plot of N vs $1/B_0$ would be expected to yield a straight line, since spin splitting is negligible at the magnetic fields encountered in the experiment. The experimental plot shown in Fig. 20, however, is not a straight line, but appears to separate into high- and low-field regions which are only roughly linear.

A straight line fitted to the high-field data of Fig. 20 has a slope which corresponds to a period of 1.8×10^{-5} G^{-1}, a value in rough agreement with the 2.07×10^{-5} G^{-1} majority hole Shubnikov–de Haas period. The line passes through four points which coincide closely with the "kinks" observed in published data of Surma, Furdyna, and Praddaude.[5] Their data, however, were not consistent enough to enable them to positively identify the features as

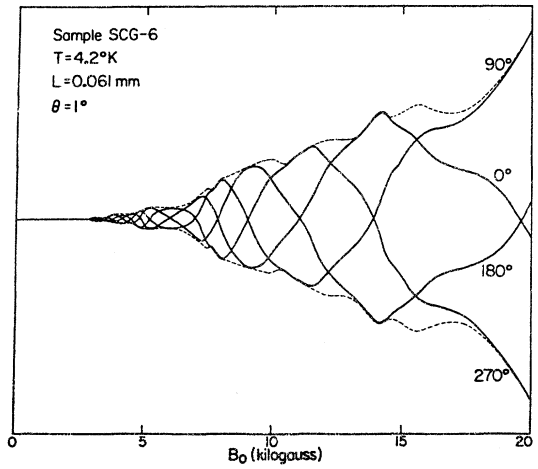

FIG. 17. Transmission interferogram and envelope for SCG-6. The envelope was determined by superposing interferograms for eight different phase settings, and is distinguished from that of the other transmission samples by a series of very pronounced "dimples."

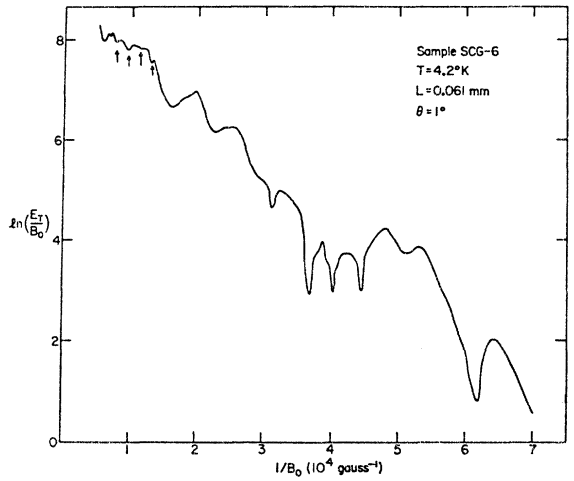

FIG. 19. Plot of $\ln E_T/B_0$ vs $1/B_0$ for SCG-6. The four arrows indicate the "kinks" in the published data of Surma, Furdyna, and Praddaude (Ref. 5), and can be seen to coincide with four successive minima in the transmission envelope.

Shubnikov–de Haas phenomena. The reason for this inconsistency may perhaps be seen in Fig. 20: There is no truly linear region in the entire magnetic field range. It is necessary to hypothesize either the presence of at least two carriers producing Shubnikov–de Haas oscillations, or a mechanism which is not linear in $1/B_0$. If Shubnikov–de Haas oscillations are assumed, the low-field data displays a period of roughly 5.9×10^{-5} G^{-1}. Although it is a bit low, this value could be associated with the oscillatory structure observed by Flood[20] and identified with the minority hole.

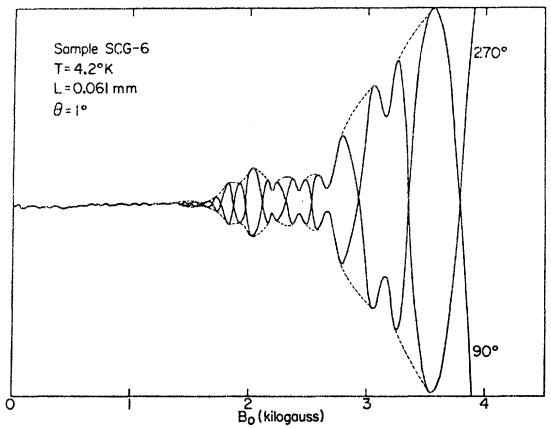

FIG. 18. Enlargement of the low-field interferogram for SCG-6. Because of a slight amount of microwave leakage, only two phase settings at a time can accurately be compared. The dimples shown, however, do not shift position as the phase setting is changed and constitute a minimum in the transmission envelope.

Alternatively, this period could be explained in terms of overlapping effects of two or more light carriers if the oscillations are to be ascribed to Shubnikov–de Haas behavior of previously observed carriers.

The phase results for this sample are presented in Fig. 21. The slope of the line drawn through the data indicates a mass density corresponding to $M=(2.36\pm0.72)\times10^{-10}$ g cm^{-3}, in agreement with the results for pyrolytic graphite (see Fig. 8). The angular dependence of the effective orientation-dependent mass density M_θ again shows a $\cos\theta$ dependence. There is a small oscillatory deviation from linearity in the high-field region of Fig. 21 which is roughly periodic in $1/B_0$ with a period of

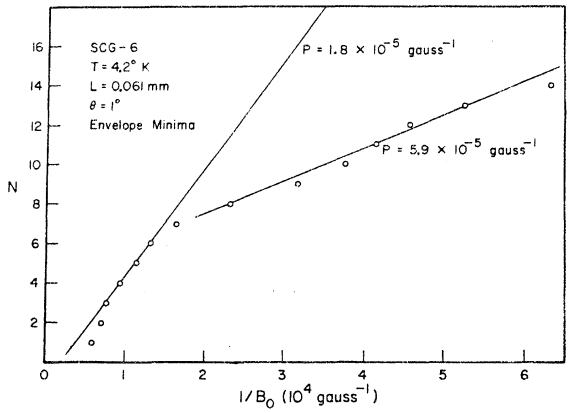

FIG. 20. Plot of successive envelope minima vs $1/B_0$. The graph is not linear, but can be approximated by two linear sections.

7.5×10^{-5} G^{-1}. This period agrees with a minority carrier Shubnikov–de Haas period reported by Flood.[20] The structure is seen more clearly in Fig. 22, which is a plot of phase vs Lf/B_0 for the high-field region of Fig. 21 for several orientations of the magnetic field. The structure tends to exhibit the same orientational dependence as the damping maxima, indicated by the arrows.

There are several possible explanations for the observed oscillatory amplitude and phase behavior: Propagation of electromagnetic waves in the Faraday geometry ($\vec{B}_0 \parallel \vec{q}$) is usually described in terms of two circularly polarized normal modes, traveling with different phase velocities and damping. In the limit of $\omega_p^2 \gg \omega_c \gg \omega \gg \nu$ and $n_e = n_h$, the behavior of the two circular modes becomes identical. The superposition of the two circularly polarized waves then produces a linearly polarized Alfvén wave. However, in the absence of total compensation, or at low fields for materials with unequal electron and hole mobilities, the two circular modes are no longer degenerate. The polarization of the transmitted wave is elliptical because of the unequal damping, and the inequality in phase velocities causes the axis of the ellipse to rotate as a function of B_0. Since the exit waveguide can accept only one linear polarization, it would "see" only the projection of the transmitted field along the direction which couples to the waveguide. The combined effect of changing ellipticity and orientation of the transmitted field pattern would result in an oscillation in the detected power.

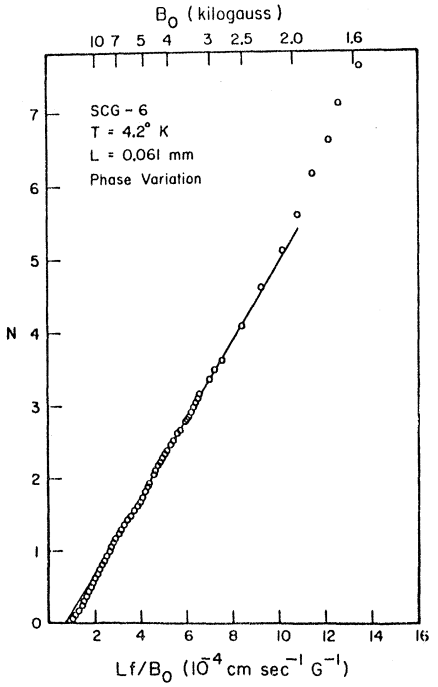

FIG. 21. Fringe index for SCG-6 vs $1/B_0$. The plot is roughly linear with a low-field deviation and a small high-field oscillatory structure. The average high-field slope is in agreement with the Alfvén-wave mass density observed in pyrolytic graphite.

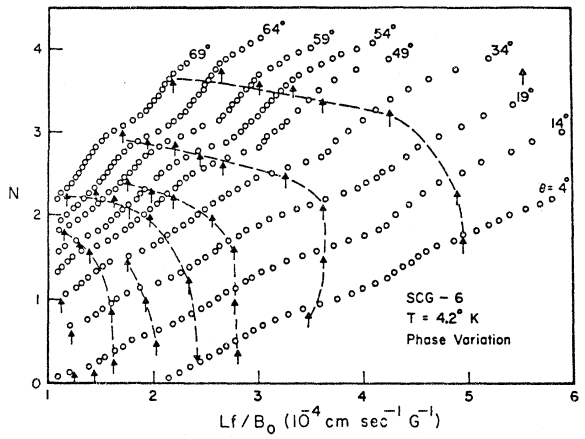

FIG. 22. Fringe index vs $1/B_0$ as the magnetic field is rotated. The arrows indicate the transmission minima and can be seen to have roughly the same angular dependence as the oscillations in fringe index, although the periods are not the same.

This mechanism could therefore be responsible for the observed transmission minima. It is difficult to see, however, how the carrier concentration would be unbalanced unless there were present donor or acceptor impurities. The presence of such impurities would not be consistent with the low collision frequency observed for the sample. Similarly, if this mechanism were associated with unequal mobilities, the effect would appear when ω_c/ν is low and would be more pronounced at low magnetic fields and in the pyrolytic samples, which have consistently higher scattering rates. The fact that the oscillations are observed at all fields, but only in a single-crystal sample with very low ν, suggests that the oscillations are not caused by changes in polarization.

The high-field transmission minima could be plausibly explained as Shubnikov–de Haas oscillations in scattering rate of the majority hole. However, since the collision frequency was lower than for most of the pyrolytic samples which did not exhibit phase oscillations, we would not expect oscillations in collision frequency to affect the phase because ν only appears in the expression for the phase as the small quantity ν^2/ω^2. Oscillations in carrier concentration would directly affect both the phase and the amplitude of the transmitted wave. This effect would be most readily observed in samples with low collision frequency, such as SCG-6. The corresponding phase and amplitude oscillations would have the same or similar periods, as is observed.

B. Reflection

Although the primary pupose of this experiment was not to investigate Shubnikov–de Haas phenomena, the anomalous results obtained with sample SCG-6 did warrant further study of single-crystal material. Because of the difficulty of obtaining large single crystals of sufficient quality, the reflection technique was used to study most of these samples. The small natural flakes could then be used almost "as is." The only preparation consisted of cleaving them to ensure planar faces and gluing them to a copper disk which formed one end of the cavity.

Such an arrangement is sensitive to both the surface (half-space) absorption and the fields transmitted through the sample. The surface absorption of a medium which is sustaining Alfvén-wave propagation increases linearly with magnetic field.[21] The transmitted signal, however, induces currents on the back face of the sample which interfere with the currents in the cavity wall. The result is much the same as that encountered using the bypass arm in the transmission experiment; constructive and destructive interference occurs as the phase of the wave emerging from the sample varies with the magnetic field. Similar experimental arrangements have been discussed by Walsh[22] and by Surma, Furdyna, and Praddaude.[5]

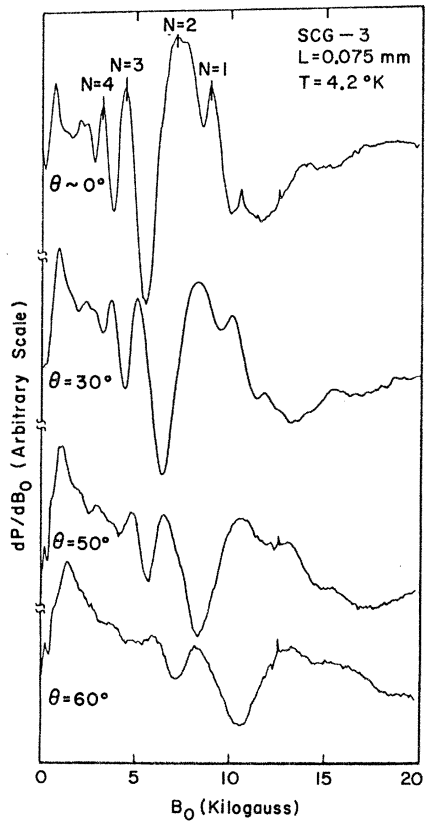

FIG. 23. Reflection data for SCG-3. The cyclotron resonance region, Alfvén-wave region, and high-field Shubnikov–de Haas region are clearly resolved.

The reflection data for a sample of single-crystal graphite is shown in Fig. 23 for several orientations of the magnetic field. The vertical axis is proportional to the derivative of the absorbed power, since field modulation was used. The structure seen between 2 and 10 kG is the Alfvén-wave interference pattern. The spacing of this structure increases as $(\cos\theta)^{-1}$ as the field is rotated, and for a given orientation varies as the inverse sample thickness. At high fields, a thick sample is desired to provide adequate phase data, but at low fields a thin sample is needed for adequate signal. The transparency of SCG-7, the thinnest sample studied by reflection, makes it possible to see transmission structure below 2 kG (Fig. 24). The appearance of this structure suggests the existence of two different regions of behavior, with the transition occurring at about 700 G. Above this field, the periodic structure is consistent with that expected for Alfvén-wave propagation.

Below 700 G, there is structure related to the harmonics of cyclotron resonance. Cyclotron resonance was also observed in the other two single-crystal samples. Although not quite as well resolved in these two samples, the structure is still unambiguous and independent of sample thickness, proving that it is a bulk property of graphite, not a transmission effect. There is one peak in Fig. 24 near 500 G at $\theta = 0°$, which does not correspond to any of the expected electron cyclotron resonance harmonics. Scaling the observed structure to a frequency of 70 GHz, this peak coincides with a similar anomalous peak appearing in the 70-GHz reflection results of Tanuma and Suematsu.[23] Uda[24] has identified the peak as the result of the electron-hole interaction.

Returning to the data above 700 G, the inverse magnetic fields at which the extrema in the oscillations occur are plotted for sample SCG-3 in Fig. 25. The ordinate counts successive maxima (or minima) starting at the high field end of the data as shown in Fig. 23. The vertical position is arbitrary. Over most of the range, the extrema display a period constant in $1/B_0$, although there is a departure from this behavior at fields in excess of 7 kG. As the angle between the magnetic field and the normal to the surface is increased, the period associated with the region linear in $1/B_0$ decreases.

Two mechanisms are expected to produce an oscillatory behavior periodic in $1/B_0$, the Shubnikov–de Haas effect and Alfvén-wave propagation. The period of the oscillations caused by the former mechanism is independent of the sample thickness

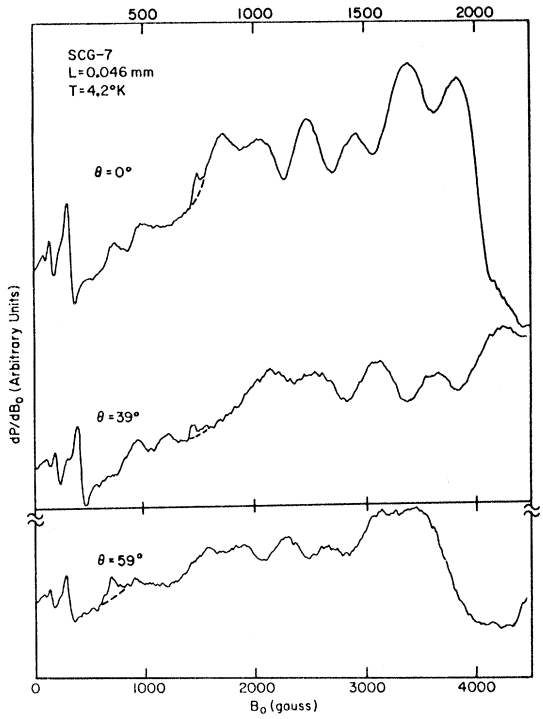

FIG. 24. Enlarged view of the low-field data for SCG-7. Cyclotron resonance is clearly seen below 700 G. The region between 700 and 2000 G is dominated by Alfvén-wave propagation. The peak at 750 G is spurious.

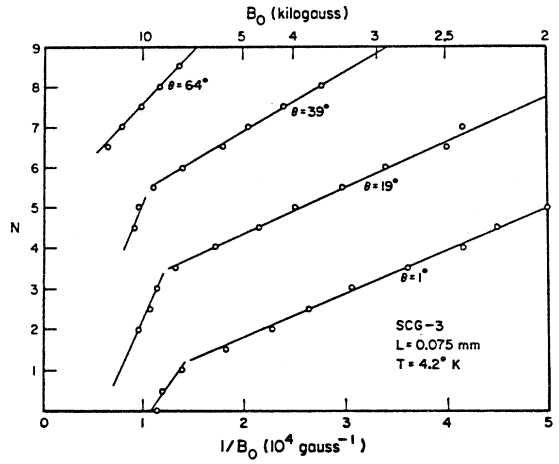

FIG. 25. Phase results for SCG-3. The successive maxima (or minima) of Fig. 23 are labeled with consecutive integers N, starting at the highest magnetic field for which an extremum is observed. There are two distinct regions. The slope of the data above 1.4×10^{-4} G^{-1} corresponds to the Alfvén-wave structure, while the slope at higher fields corresponds roughly to the majority-hole Shubnikov–de Haas resonance period.

and related uniquely to the extremal mass of a given carrier species, while the period associated with the latter mechanism is inversely proportional to the sample thickness and related to the integrated cyclotron mass. Both periods vary as $(\cos\theta)^{-1}$. Denoting the period in $1/B_0$ as P, it can be shown that for Alfvén-wave propagation, the plot in Fig. 25 should be a straight line with slope P^{-1} related to the integrated mass density by the expression

$$(\mu_0 M)^{1/2} = 1/LfP \ . \tag{20}$$

The period observed in Fig. 25 does not correspond to any of the expected Shubnikov–de Haas periods, but the quantity $1/LfP$ does give reasonable agreement with the calculated Alfvén-wave mass density. There is not enough information in the region above 7 kG where the data depart from linearity to accurately determine the behavior there. However, the slope of a straight line fit through the last three points is in rough agreement with the Shubnikov–de Haas periods of the majority carriers. The experiments by Soule, McClure, and Smith,[10] by Woollam,[25] and by Furdyna and Krauss[6] indicate that Shubnikov–de Haas oscillations associated with the electron Fermi surface are not seen below 10 kG, and any Shubnikov–de Haas structure in Fig. 25 would consequently be associated with the majority holes.

Two distinct regions are also observed in sample SCG-2 (Fig. 26). Here, however, the high-field region is associated with Alfvén waves while the low-field region has a very long period. Interpreting the long period as a Shubnikov–de Haas oscillation, the corresponding extremal mass is very light, roughly in agreement with the minority carrier mass reported by Soule.[26]

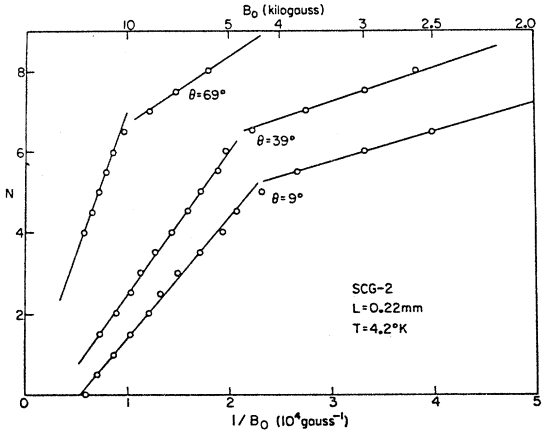

FIG. 26. Phase results for SCG-2. There are two distinct regions. The slope of the data below 2.3×10^{-4} G^{-1} corresponds to Alfvén-wave behavior, and the slope above this region is in agreement with the minority-carrier Shubnikov–de Haas period observed by Soule (Ref. 26).

There is a common source of error inherent in all measurements of periods obtained from the reflection data. The measurements are based on the observed positions of the extrema. If the extrema are imposed upon a changing background (arising, e.g., from the variation of the Alfvén-wave amplitude), the observed positions will be shifted from the positions which they would occupy if the background were constant. This difficulty is not present in the transmission experiment.

The orientational behavior of the Alfvén-wave period is shown in Fig. 27. The coordinate axis is normalized to the period P_0, corresponding to $\theta = 0°$, to permit direct comparison of the three samples. To within the extent of the experimental scatter, the data display a $\cos\theta$ dependence.

Figure 28 exhibits the angular dependence of the minority carrier period for SCG-2. The data again exhibit a $\cos\theta$ dependence. The minority hole ellipsoid anisotropy ratio has been measured by Soule as 9:1. While this is not as extreme as the value of 12.1:1 for the majority surfaces, it is still large enough to produce essentially a $\cos\theta$ dependence at the largest angles for which the oscillation was observable in the present experiment.

The reflection results for three single-crystal samples at fields greater than 700 G are given in Table I for the geometry $\vec{B}_0 \| \vec{c}$. The experimental mass densities are lower than the values measured in transmission. This result is to be expected since the interference pattern is imposed upon a rising background. In the Alfvén-wave reflection experiments of Tanuma and Suematsu[23] it was found that the observed mass density required thicknesses of as much as 40% less than the measured values to fit the theory. The three experimental values are quite consistent with each other, indicating that the spacing of the observed structure is inversely proportional to sample thickness and therefore corresponds to a transmission phenomenon rather than to sample reflectivity.

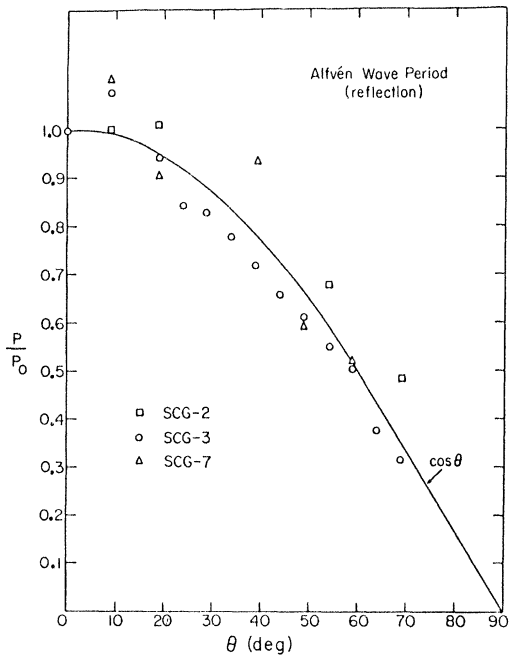

FIG. 27. Alfvén-wave period as a function of orientation. P_0 is the period for $\theta = 0°$. The normalized period varies as a $\cos\theta$ out to 70°, the largest angle at which quantitative data were obtainable.

C. Summary and Remarks

A summary of the experimental results are presented in Table I. The average value of the mass

TABLE I. Results for single-crystal and pyrolytic samples for the geometry $\vec{B}_0 \| \vec{c}$.

Sample	Thickness (mm)	Temp. (°K)	M (g cm^{-3}) ($\times 10^{-10}$)	ν_s (sec^{-1})	Short oscillatory period (10^{-5} G^{-1})	Long oscillatory period (10^{-5} G^{-1})	Method
PGA-17	0.130	4.2	1.96	4.4×10^{10}			Transmission
PGA-18	0.100[a]	4.2		4.0×10^{10}			
PGA-19	0.036	4.2	2.66	5.8×10^{10}			
PGA-20	0.072	4.2	2.07	8.3×10^{10}			
PGA-21	0.024	4.2	2.92	8.5×10^{10}			
PGA-22	0.011[a]	4.2		1.52×10^{11}			
PGA-24	0.010[a]	4.2		3.04×10^{11}			
		77	4.08	4.42×10^{11}			
SCG-6	0.061	4.2	2.28	3.85×10^{10}	1.8	5.9 7.5[b]	
SCG-2	0.220	4.2	1.23			13.0	Reflection
SCG-3	0.075	4.2	1.30		2.67		
SCG-7	0.046	4.2	1.42				
Theoretical (Ref. 11)			3.22				

[a]Sample thickness determined from phase data.

[b]Phase oscillation.

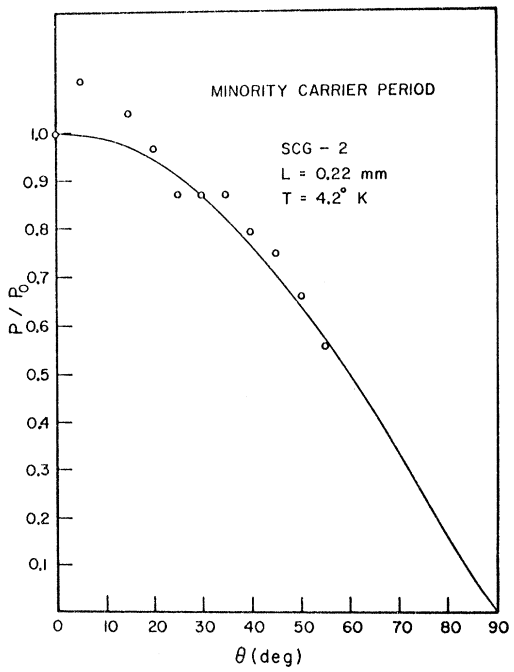

FIG. 28. Orientational dependence of the minority carrier period of SCG-2. The normalized period varies as $\cos\theta$ out to 55°, indicating a highly anisotropic Fermi surface.

density obtained in transmission, $(2.38 \pm 0.40) \times 10^{-10}$ g cm^{-3}, is in fair agreement with the earlier value obtained in the high-field transmission experiments of Furdyna and Krauss[6] (1.83×10^{-10} g cm^{-3}). Both experimental values, however, are below that obtained from the integrated mass density calculated by Dresselhaus and Dresselhaus,[11] 3.22×10^{-10} g cm^{-3}. The difference corresponds to an error in sample thickness of approximately 10%. The published thermal-expansion coefficients for graphite[27] indicate that the sample contraction when immersed in liquid helium is far less than this amount. The presence of microcracks between basal plane layers would cause the optical thickness to be less than the mechanical thickness and could also be responsible for the high anisotropy in collision rate observed by Spain. A different procedure which determined sample *optical* thickness should be used in future experiments to resolve this question.

The damping exhibited departures from the behavior expected on the basis of a single field-independent effective collision frequency, although the nature of the departure differed from sample to sample. Consequently, no firm conclusions could be drawn with regard to the field dependence.

A comparison of Tables I and II reveals that the short oscillatory periods of samples SCG-6 and SCG-3 agree with the majority-hole Shubnikov–de Haas damping while the long-period oscillations generally agree with the various values for the minority hole. A phase oscillation was observed upon transmission through SCG-6 with a period again corresponding roughly to that of the minority hole. No structure was observed corresponding to the reported minority electron period.

ACKNOWLEDGMENTS

The authors would like to thank Professor S. Tanuma and Dr. H. Suematsu for communicating their results prior to publication. They are further indebted to Dr. J. A. Woollam for providing the pyrolytic graphite and to Professor M. Dresselhaus and Dr. G. L. Montet for the single-crystal material.

APPENDIX: DIELECTRIC CONSTANT

It is assumed that both the effective mass and the collision frequency can be described by an ellipsoidal model with principal values m_x, m_y, m_z and ν_x, ν_y, ν_z, where the z axis is taken to be along the hexagonal symmetry axis. The wave is also assumed propagating along the z axis, as it does, in fact, propagate in graphite, and the dc magnetic field is taken to be in the x-z plane. Each carrier is then described by the equation of motion, Eq. (2). Because of the symmetry about the z axis, it can be assumed that $\nu_x = \nu_y = \nu_t$, $\nu_z = \nu_l$, $m_x = m_y = m_t$, and $m_z = m_l$, where the subscripts t and l stand for "transverse" and "longitudinal," respectively. Solving Eq. (2) for the velocity, the conductivity corresponding to a single carrier may be written

$$\vec{\vec{\sigma}} = \frac{ne^2}{D} \begin{pmatrix} e^2B_0^2\sin^2\theta + \gamma_t\gamma_l & QB_0\gamma_l\cos\theta & e^2B_0^2\sin\theta\cos\theta \\ -QB_0\gamma_l\cos\theta & \gamma_t\gamma_l & QB_0\gamma_t\sin\theta \\ e^2B_0^2\sin\theta\cos\theta & -QB_0\gamma_t\sin\theta & e^2B_0^2\cos^2\theta + \gamma_t^2 \end{pmatrix} , \tag{A1}$$

where

$$\gamma_t = (\nu_t + i\omega)m_t , \quad \gamma_l = (\nu_l + i\omega)m_l ,$$

and

$$D = \gamma_t^2\gamma_l + e^2B_0^2[\gamma_t\sin^2\theta + \gamma_l\cos^2\theta] .$$

For a two-carrier medium, the conductivity con-

TABLE II. Observed Shubnikov–de Haas periods.

Carrier	Period (G^{-1})	Ellipsoid anisotropy	Observer (Refs.)
Majority electron	1.51×10^{-5}	12.1	10
Majority hole	2.07×10^{-5}	12.1	10
Minority hole	1.35×10^{-4}	9	26
	2.2×10^{-4}	1.9	28
	$(0.85\pm0.2)\times10^{-4}$	...	20
	1.1×10^{-4}	>13	29
Minority electron(?)	$\geq 2.5\times10^{-4}$	...	26
	2.9×10^{-4}	2.3	28, 29

sists of two terms of the form of Eq. (A1). The dielectric constant for such a system is given by the expressions

$$K_{xx} = K_L + \frac{n_h e^2}{D_h i\omega\epsilon_0}(e^2B_0^2\sin^2\theta + \gamma_{th}\gamma_{lh}) + \frac{n_e e^2}{D_e i\omega\epsilon_0}(e^2B_0^2\sin^2\theta + \gamma_{te}\gamma_{le}) ,$$

$$K_{xy} = \frac{n_h e^2}{D_h i\omega\epsilon_0}(eB_0\gamma_{lh}\cos\theta) - \frac{n_e e^2}{D_e i\omega\epsilon_0}(eB_0\gamma_{le}\cos\theta) ,$$

$$K_{xz} = \left(\frac{n_h e^2}{D_h i\omega\epsilon_0} + \frac{n_e e^2}{D_e i\omega\epsilon_0}\right) e^2B_0^2\sin\theta\cos\theta ,$$

$$K_{yx} = -K_{xy} ,$$

$$K_{yy} = K_L + \frac{n_h e^2}{D_h i\omega\epsilon_0}\gamma_{th}\gamma_{lh} + \frac{n_e e^2}{D_e i\omega\epsilon_0}\gamma_{te}\gamma_{le} ,$$

$$K_{yz} = \left(\frac{n_h e^2}{D_h i\omega\epsilon_0}\gamma_{th} - \frac{n_e e^2}{D_e i\omega\epsilon_0}\gamma_{te}\right) eB_0\sin\theta ,$$

$$K_{zx} = K_{xz} , \quad K_{zy} = -K_{yz} ,$$

$$K_{zz} = K_L + \frac{n_h e^2}{D_h i\omega\epsilon_0}(e^2B_0^2\cos^2\theta + \gamma_{th}^2) + \frac{n_e e^2}{D_e i\omega\epsilon_0}(\epsilon^2B_0^2\cos^2\theta + \gamma_{te}^2) ,$$

where the additional subscripts e and h refer to electrons and holes.

Effective Collision Frequency

It has been assumed in the body of the text that holes and electrons have the same collision frequency. Although mobility measurements indicate that this condition is roughly true, it should not be assumed *a priori*. However, for describing Alfvén-wave propagation and damping, it is adequate to use a single "effective" collision frequency for both carriers. To see why, it is convenient to consider the high-field isotropic case.

For a compensated medium, Eqs. (4) and (A2) yield the dispersion relation

$$q^2 = \frac{\omega^2}{c^2}n\frac{m_e+m_h}{\epsilon_0B_0^2} - i\frac{\omega^2}{c^2}n\frac{m_e\nu_e+m_h\nu_h}{\omega\epsilon_0B_0^2} . \tag{A3}$$

This expression is equivalent to Eq. (8) if the quantity ν is defined as an "average" collision frequency:

$$\nu = (m_e\nu_e + m_h\nu_h)/(m_e+m_h) . \tag{A4}$$

Since the Alfvén-wave behavior depends only on this average value, the hybrid parameter ν may be taken as the characteristic collision frequency for the medium.

Cylindrical Fermi Surface

The dispersion relation for an anisotropic medium resulting from Eqs. (1) and (A2) are, in general, rather cumbersome. Simplification results of course when the isotropic model is assumed. It is also possible to find a simple expression for the dispersion relation in the case of the cylindrical Fermi surface, which in many respects provides a good approximation to the case of graphite.

The cylindrical Fermi surface may be considered as an ellipsoid with infinite longitudinal mass, and the previous results for an anisotropic medium may be carried over directly. Trouble arises, however, if one immediately sets $m_l = \infty$ in Eq. (A2). It is convenient to rewrite the free-carrier terms of (A2) in the high-field collisionless limit for each single carrier as

$$\begin{aligned}
K_{xx} &= -(\omega_p^2/\omega^2)\tan^2\theta + (\omega_p^2/\omega_c^2)R ,\\
K_{xy} &= -iR\omega_p^2/\omega\omega_c = -K_{yx} ,\\
K_{xz} &= -(\omega_p^2/\omega^2)\tan\theta = K_{zx} ,\\
K_{yy} &= R\omega_p^2/\omega_c^2 ,\\
K_{yz} &= -i(\omega_p^2/\omega\omega_c)\tan\theta = -K_{zy} ,\\
K_{zz} &= \omega_p^2/\omega_c^2 - \omega_p^2/\omega^2 ,
\end{aligned} \tag{A5}$$

where $R = m_l/m_t$ is the mass anisotropy ratio, $\omega_p = (ne^2/m_l\epsilon_0)^{1/2}$ is the plasma frequency, $\omega_c = eB_0/m_c$ is the cyclotron frequency, and m_c is the cyclotron effective mass, which has been here defined as

$$m_c = m_t/\cos\theta \tag{A6}$$

as required for a cylindrical Fermi surface.

It will be assumed that both electrons and holes have the same mass anisotropy and exist in equal concentrations ($n_e = n_n = n$). The condition $K_{xy} = K_{yx} = K_{yz} = K_{zy} = 0$ results from the equality of carrier concentrations. It is convenient to define the quan-

tities

$$S=\omega_{pe}^2/\omega_{ce}^2+\omega_{ph}^2/\omega_{ch}^2\,,$$
$$T=(\omega_{pe}^2+\omega_{ph}^2)/\omega^2\,, \tag{A7}$$

where the subscripts e and h once again refer to electrons and holes. The dielectric constant then has the form

$$K_{xx}=RS-T\tan^2\theta\,,\quad K_{xz}=-T\tan\theta\,,$$
$$K_{yy}=RS\,,\quad K_{zz}=S-T\,. \tag{A8}$$

The resulting dispersion relation has two solutions,

$$\eta_+^2=K_{yy}=RS=\frac{n(m_{te}+m_{th})}{\epsilon_0 B_0^2}\,\frac{1}{\cos^2\theta}\,, \tag{A9}$$

$$\eta_-^2=K_{xx}-\frac{K_{xz}^2}{K_{zz}}=S\,\frac{R(S-T)-T\tan^2\theta}{S-T}\,. \tag{A10}$$

Because Eq. (A5) is based on the high-field approximation ($\omega/\omega_c\ll 1$), the condition $S\ll T$ is satisfied. It may also be assumed for graphite that $R\gg\tan^2\theta$ for all angles except $\theta\approx 90°$. Equation (A10) then reduces to Eq. (A9). The longitudinal mass has dropped out during the course of the calculation, thereby eliminating any singularities. Defining the transverse mass density parameter M_t as

$$M_t=n(m_{te}+m_{th})\,, \tag{A11}$$

the dispersion relation becomes

$$q_\pm^2=\omega^2\mu_0 M_t/B_0^2\cos^2\theta\,. \tag{A12}$$

The same expression was derived for the slow Alfvén wave in an isotropic medium with effective masses equal to the transverse masses used to characterize the cylindrical medium. The present result occurs because the extremely large longitudinal mass corresponds to a very low mobility and does not give rise to significant transport phenomena. Since Alfvén-wave propagation depends only on the carrier velocity components perpendicular to $\vec{B}_0$, the transverse mass enters with a $\cos\theta$ dependence. The Alfvén-wave velocity as calculated from Eq. (A12) and by using the exact dispersion relation based on Eq. (A2) for a 12:1 ellipsoid ratio is shown in Fig. 2(d). The two plots are indistinguishable, providing a striking demonstration of the anisotropic nature of graphite.

---

*Supported by the Advanced Research Projects Agency and the National Science Foundation.

†Present address: James Franck Institute, The University of Chicago, Chicago, Ill. 60637.

[1]H. Alfvén, Nature (Lond.) **150**, 405 (1942).
[2]G. A. Williams, Bull. Am. Phys. Soc. **7**, 409 (1962).
[3]R. T. Isaacson and G. A. Williams, Phys. Rev. Lett. **22**, 26 (1969).
[4]R. T. Isaacson and G. A. Williams, Phys. Rev. **185**, 682 (1969).
[5]M. Surma, J. K. Furdyna, and H. C. Praddaude, Phys. Rev. Lett. **13**, 710 (1964).
[6]J. K. Furdyna and A. R. Krauss, in *Proceedings of the Conference of Physics of Semimetals and Narrow Gap Semiconductors, Dallas, Texas, 1970* (Pergamon, England, 1971).
[7]W. P. Allis, S. J. Buchsbaum, and A. Bers, *Waves in Anisotropic Plasmas* (MIT Press, Cambridge, Mass., 1963).
[8]J. W. McClure (private communication).
[9]E. A. Kaner and V. G. Skobov, Adv. Phys. **17**, 605 (1968); see, also, J. K. Furdyna, Appl. Opt. **6**, 675 (1967).
[10]D. E. Soule, J. W. McClure, and L. B. Smith, Phys. Rev. **134**, A453 (1963).
[11]M. S. Dresselhaus and G. F. Dresselhaus, Lincoln Laboratory Quarterly Report No. 3, 1964 (unpublished), p. 40.
[12]I. L. Spain, in Ref. 6.
[13]J. K. Furdyna and A. R. Krauss, Phys. Rev. B **2**, 3183 (1970).
[14]J. K. Furdyna, Rev. Sci. Instrum. **37**, 462 (1966).
[15]T. A. Evans, Ph.D. thesis (Purdue University, 1971) (unpublished).
[16]J. W. McClure, Phys. Rev. **112**, 715 (1958).
[17]D. E. Soule, Phys. Rev. **112**, 698 (1958).
[18]O. S. Heavens, *Optical Properties of Thin Solid Films* (Dover, New York, 1965), pp. 51–54.
[19]E. H. Marston and Y.-H. Kao, Phys. Kondens. Mater. **9**, 195 (1969).
[20]D. J. Flood, Phys. Lett. A **30**, 178 (1968).
[21]S. J. Buchsbaum and J. K. Galt, Phys. Fluids **4**, 1514 (1961).
[22]W. M. Walsh, Jr., in *Solid State Physics*, edited by J. Cochran and R. Haering (Gordon and Breach, New York, 1968), Vol. 1.
[23]S. Tanuma and H. Suematsu (private communication).
[24]R. Uda, Ph.D. thesis (University of Tokyo, 1971) (unpublished).
[25]J. A. Woollam, Phys. Lett. A **32**, 371 (1970).
[26]D. E. Soule, IBM J. Res. Dev. **8**, 268 (1964).
[27]S. P. Clark, Jr., *Handbook of Physical Constants* (Geological Society of America, New York, 1966).
[28]S. J. Williamson, S. Foner, and M. S. Dresselhaus, Phys. Rev. **140**, A1429 (1965).
[29]J. A. Woollam, Phys. Rev. B **4**, 3393 (1971); and private communication.